ADVANCED SCIENCE Open Access
www.advancedscience.com

High-Performance Semitransparent Organic Solar Cells: From Competing Indexes of Transparency and Efficiency Perspectives

Tao Xu, Yiran Luo, Shiwei Wu, Baozhong Deng, Shi Chen, Yunbo Zhong, Shenghao Wang,* Gaëtan Lévêque, Renaud Bachelot, and Furong Zhu**

Semitransparent organic solar cells (ST-OSCs) offer potentially more opportunities in areas of self-powered greenhouses and building-integrated photovoltaic systems. In this work, the effort to use a combination of solution-processable gold nanobipyramids (AuNBPs)-based hole transporting layer and a low/high dielectric constant double layer optical coupling layer (OCL) for improving the performance of ST-OSCs over the two competing indexes of power conversion efficiency (PCE) and average visible transmittance (AVT) is reported. The fabrication and characterization of the ST-OSCs are guided, at design and analyses level, using the theoretical simulation and experimental optimization. The use of a low/high dielectric constant double layer OCL helps enhancing the visible light transparency while reflecting the near-infrared (NIR) photons back into the photoactive layer for light harvesting. NIR absorption enhancement in the ST-OSCs is realized through the AuNBPs-induced localized surface plasmon resonance (LSPR). The weight ratio of the polymer donor to nonfullerene acceptor in the bulk heterojunction is adjusted to realize the maximum NIR absorption enhancement, enabled by the AuNBPs-induced LSPR, achieving the high-performance ST-OSCs with a high PCE of 13.15% and a high AVT of 25.9%.

1. Introduction

Organic solar cells (OSCs) offer an attractive option for achieving low-cost and clean energy sources.[1–6] OSCs can be made flexible and semitransparent. The unique flexibility and semi-transparency feature of the OSCs also add a decorative and aesthetic dimension to the solar cells so that they can be used on curved and irregular surfaces, which cannot be done using traditional rigid silicon solar cells. Power conversion efficiency (PCE) of >18% has been realized for the OSCs using the blends of the low bandgap polymer and nonfullerene acceptors (NFAs), having good electron mobility, tunable energy levels, and an extended absorption in the near-infrared (NIR) region.[7–14] The development of semitransparent OSCs (ST-OSCs) is still in its development stage, particularly the design and optimization of cell performance over the two competing indexes of PCE and average visible transmittance (AVT).

T. Xu, Y. Luo
School of Mechatronic Engineering and Automation
Shanghai University
Shanghai 200444, China

S. Wu, B. Deng, Y. Zhong
School of Materials Science and Engineering
Shanghai University
Shanghai 200444, China
E-mail: yunboz@shu.edu.cn

S. Chen, S. Wang
Materials Gerome Institute
Shanghai University
Shanghai 200444, China
E-mail: shenghaowang@shu.edu.cn

G. Lévêque
Université de Lille
CNRS
Centrale Lille
Université Polytechnique Hauts-de-France
ISEN-Yncrea Hauts-de-France, UMR 8520 – IEMN, Lille 59000, France

R. Bachelot
Light, nanomaterials, nanotechnologies (L2n)
CNRS ERL 7004
University of Technology of Troyes
Troyes Cedex F-10004, France

F. Zhu
Department of Physics
Research Centre of Excellence for Organic Electronics and Institute of Advanced Materials
Hong Kong Baptist University
Kowloon Tong, Hong Kong 999077, China
E-mail: frzhu@hkbu.edu.hk

The ORCID identification number(s) for the author(s) of this article can be found under https://doi.org/10.1002/advs.202202150

DOI: 10.1002/advs.202202150

The ST-OSC technology can be advanced through new materials development, including new low bandgap polymers and NFAs with enhanced absorption in NIR region, for applications in mobile electronics, smart sensors, automotive, power generating windows, building-integrated photovoltaic, and self-powered greenhouse.[15–18]

Much effort has been devoted to develop new active layer materials with extended absorption in NIR region,[19–21] for example, using ternary strategy with two compatible NFAs,[22–24] optimizing the bulk heterojunction (BHJ) absorption for improved spectral response over the long wavelengths,[25,26] and incorporating the desired optical coupling layers (OCLs) with the upper transparent electrodes.[27–30] ST-OSCs with a PCE of ≈13% and an AVT of ≈20% have been reported.[31–35] Achieving NIR absorption enhancement in ST-OSCs based on different light trapping features has been proposed, for example, using metal nanostructures (MNS) to achieve NIR absorption enhancement in ST-OSCs through the localized surface plasmon resonance (LSPR).[36–41] The peak wavelength of the MNS-induced LSPR can be adjusted by tuning the size, shape, and composition of the MNS.[42,43] Incorporation of the MNS with optimized size and the shape for NIR absorption enhancement in ST-OSCs can be guided by the simulations. The peak wavelength and the strong local electric field of the LSPR generated by the gold nanobipyramids (AuNBPs) can be adjusted accordingly over the wavelength region from 700 to 1000 nm,[44,45] for achieving NIR absorption enhancement in ST-OSCs.

Omnidirectional absorption enhancement in OSCs incorporating 2D photonic structures, through combined effects of light scattering, excitation of surface plasmon polaritons, waveguide modes, and their mutual coupling, has been reported.[46] The introduction of a Bragg reflector, comprising multiple layers of alternating materials with varying refractive index for increasing absorption of NIR photons in ST-OSCs, has been demonstrated.[47–50] In a previous work, we analyzed the performance of the ST-OSCs using a bilayer metal/indium tin oxide (ITO) transparent electrode. The use of a low processing temperature ITO upper contact enhances the performance of ST-OSCs in two ways: 1) it helps to improve the lateral conductivity of the transparent electrode, and 2) it also serves as an index matching layer to increase the visible light transparency.[51] However, a systematic study on improving the performance of ST-OSCs over the two competing indexes of PCE and AVT is rather rare.

In this work, we report our effort to use a solution-processable AuNBPs-based hole transporting layer (HTL) and a low/high dielectric constant LiF/MoO_3 double layer OCL to optimize the performance of the ST-OSCs over the two competing indexes of AVT and PCE. The BHJ comprises a blend layer of poly[[4,8-bis[5-(2-ethylhexyl)-4-fluoro-2-thienyl]benzo[1,2-b:4,5-b′]dithiophene-2,6-diyl]-2,5-thiophenediyl[5,7-bis(2-ethylhexyl)-4,8-dioxo-4H,8H-benzo[1,2-c:4,5-c′]dithiophene-1,3-diyl]-2,5-thiophene diyl](PM6) polymer donor and an NFA 2,2′-[[12,13-bis(2-butyloctyl)-12,13-dihydro-3,9-dinonylbisthieno[2″,3″:4′,5′] thieno[2′,3′:4,5]pyrrolo[3,2-e:2′,3′-g][2,1,3] benzothiadiazole-2,10-diyl]bis[methylidyne(5,6-chloro-3-oxo-1H-indene-2,1(3H)-diylidene)]]bis[propanedinitrile] (BTP-eC9). The weight ratio of PM6 to BTP-eC9 in the BHJ and the content of the AuNBPs in the hybrid poly(3,4-ethylenedioxythiophene):poly(styrene sulfonate) (PEDOT:PSS)-AuNBPs HTL were optimized for realization of NIR absorption enhancement, and thereby the simultaneously improving the PCE and AVT of the ST-OSCs. NIR absorption enhancement in the AuNBPs-based ST-OSCs with a bilayer dielectric LiF/MoO_3 OCL was analyzed using a combination of the finite elements method (FEM) simulation and experimental optimization, achieving a high PCE of 13.15% and a high AVT of 25.9%.

2. Results and Discussion

The PM6 layer has a strong absorption in the visible range with a maximum absorption peak at 620 nm, while the BTP-eC9 layer has a complementary absorption in the long wavelength region from 600 to 1000 nm, with an absorption peak at 829 nm. The normalized absorption spectra of the donor PM6 (black curve) and the NFA BTP-eC9 (blue curve) are shown in **Figure 1**a. The geometrical parameters of AuNBPs used in in this work were designed for giving a tailored LSPR peak position at 825 nm, as shown in the extinction spectra (red curve) of Figure 1a. The LSPR peak position of the AuNBPs has been adjusted to match with the main absorption peak of BTP-eC9, for taking the advantage of enhanced NIR absorption by the BTP-eC9 acceptor molecules in the BHJ layer. The weight ratio of PM6 to BTP-eC9 in the BHJ layer and the concentration of the AuNBPs in the HTL were optimized for improving the performance of the ST-OSCs over the two competing indexes of PCE and AVT. The normalized absorption spectra measured for the PM6:BTP-eC9-blend layers prepared using the precursor solutions with different weight ratios of PM6 to BTP-eC9 are shown in Figure 1b, revealing that the absorption of the BHJ layers over the NIR region increases with the weight ratio of BTP-eC9 in the blend layer. The surface morphology of the PM6:BTP-eC9 blend layers with different weight ratios of PM6 to BTP-eC9 was analyzed using the atomic force microscopy (AFM) measurements. A fiber-like feature structure in the blend film with a weight ratio of PM6 to BTP-eC9 of 1:1.2 can be observed, as shown in Figure S1, Supporting Information, formed due to the phase separation. The root-mean-square (RMS) roughness values of 1.07 to 1.56, 2.15, and 4.42 nm were obtained for the PM6:BTP-eC9 blend films with different weight ratios of PM6 to BTP-eC9 of 1:1.2 to 0.8:1.2, 0.6:1.2, and 0.4:1.2, revealing the presence of the phase separation and oversized domains due to the stronger aggregation of BTP-eC9 molecules in the blend layer.[52]

A set of ST-OSCs prepared using BHJ with different weight ratios of PM6 to BTP-eC9 and an ultrathin Au/Ag upper semitransparent electrode was made. A 40 nm thick HTL and an 8.0 nm thick $C_{26}H_{20}N_2$ 2,9-dimethyl-4,7-diphenyl-1,10-phenanthroline (BCP) electron transporting layer (ETL) were used to improve the exciton dissociation probability. The thickness of PM6:BTP-eC9 active layer was kept at 120 nm. Reference opaque OSCs with a layer configuration of ITO/PEDOT:PSS (40 nm)/PM6:BTP-eC9 (120 nm)/BCP (8.0 nm)Al (100 nm) were fabricated for process monitoring. A summary of the short circuit current density (J_{SC}), open circuit voltage (V_{OC}), fill factor (FF), and PCE measured for the reference opaque OSCs and the control ST-OSCs, prepared using BHJ layers having different weight ratios of PM6 to BTP-eC9, is listed in **Table 1**. The performance of the opaque reference OSCs, having a PCE of 17.25%, a J_{SC} of 26.43 mA cm^{-2}, a V_{OC} of 0.85 V, and an FF of 76.6%, which is consistent with that of the previous report.[53] The current density–voltage ($J–V$) char-

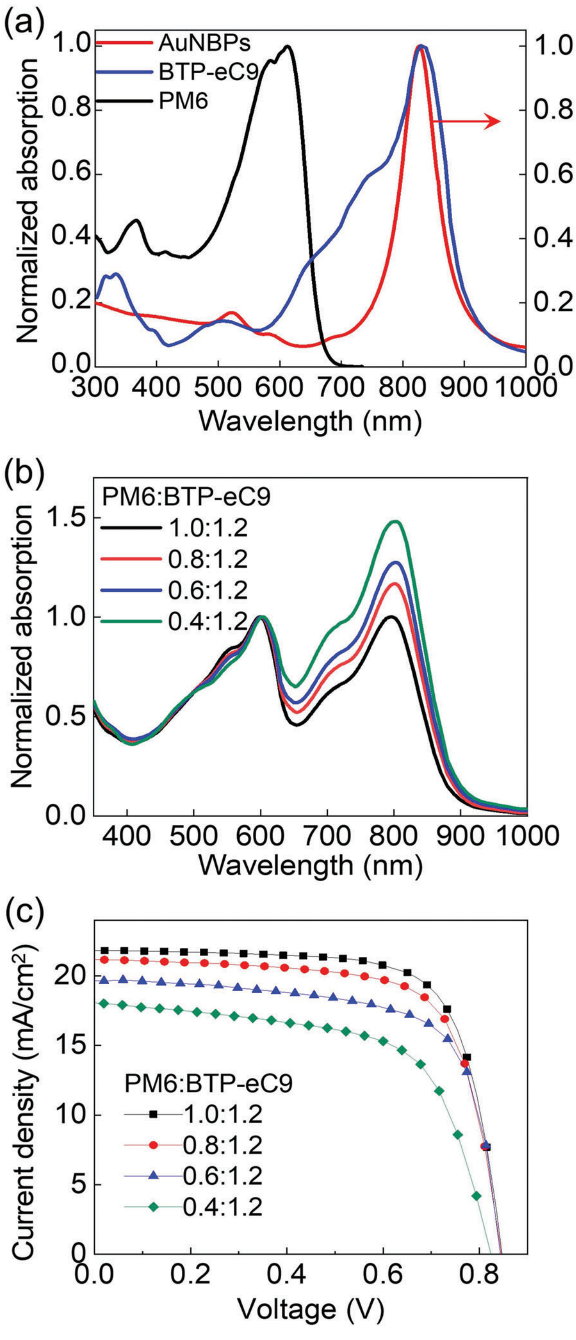

Figure 1. a) Normalized absorption spectra of PM6 and BTP-eC9 films, and extinction spectra of AuNBPs (red curve). b) Normalized absorption spectra of PM6:BTP-eC9 blend films with different weight ratios of PM6 to BTP-eC9. c) *J–V* characteristics measured for the ST-OSCs with BHJ having different weight ratios of PM6 to BTP-eC9.

acteristics and external quantum efficiency (EQE) spectra measured for the opaque OSCs prepared using the precursor solutions with different weight ratios of PM6:BTP-eC9 are shown in Figure S2, Supporting Information. A bilayer upper semitransparent contact of Au/Ag was used in the ST-OSCs. The use of a 1.0 nm thick Au interlayer was to allow forming a uniform ultrathin Ag upper electrode. The *J–V* characteristics and transparency spectra measured for the ST-OSCs, prepared using the BHJ having a weight ratio of PM6:BTP-eC9 of 1.0:1.2, with an upper Au (1.0 nm)/Ag having different Ag layer thicknesses are shown in Figure S3, Supporting Information. A summary of the corresponding cell parameters is listed in Table S1, Supporting Information. AVT of the ST-OSCs can be calculated according to the following equation:

$$\mathrm{AVT}=\frac{\int T(\lambda)\,V(\lambda)\,\mathrm{AM\ 1.5\ G}(\lambda)\mathrm{d}\lambda}{\int V(\lambda)\,\mathrm{AM\ 1.5\ G}(\lambda)\mathrm{d}\lambda} \tag{1}$$

where $T(\lambda)$ is the transparency spectrum, $V(\lambda)$ is the spectral luminous-efficiency function of the human eye, and AM 1.5 G(λ) is the photo flux of the AM 1.5 G irradiation. In this work, a bilayer upper contact of Au (1.0 nm)/Ag (10 nm) was used.

J–V characteristics measured for a set of the ST-OSCs with a PEDOT:PSS HTL, having the BHJ layer prepared using different weight ratios PM6 to BTP-eC9 of 1:1.2, 0.8:1.2, 0.6:1.2, and 0.4:1.2 are shown in Figure 1c. A highest PCE of 13.36%, along with a J_{SC} of 21.83 mA cm^{-2}, a V_{OC} of 0.85 V, an FF of 72.26%, and an AVT of 18.8% were obtained for the ST-OSCs made with a BHJ having a weight ratio of PM6 to BTP-eC9 of 1:1.2. The corresponding visible light transparency and EQE spectra of the ST-OSCs are shown in Figure S4a,b, Supporting Information.

It becomes clear that the PCE and AVT of the ST-OSCs are the two competing indexes. The LUE, a figure of merit, can be adopted to assist in analyzing the performance of the ST-OSCs. LUE is defined by:

$$\mathrm{LUE}=\mathrm{PCE}\times\mathrm{AVT} \tag{2}$$

LUE varies with the weight ratio of the PM6 to BTP-eC9 used in the BHJ in the ST-OSCs, as shown in **Figure 2**a. It shows clearly that the highest LUE of 2.82% is obtained for the ST-OSCs made with a BHJ having a weight ratio of PM6 to BTP-eC9 of 0.6:1.2. An AVT of 24.6%, close to the benchmarking value of 25%, is obtained for the ST-OSCs prepared with a BHJ having a weight ratio of PM6 to BTP-eC9 of 0.6:1.2. In addition to the PCE and AVT, the color perception of the ST-OSCs is also a critical factor in practical application,[54] which can be presented using (x,y) coordinates on the Commission Internationale de l' Éclairage (CIE) chromaticity diagram. The CIE (x,y) coordinates of the ST-OSCs can be calculated using the transmission spectra. As shown in Figure S4c, Supporting Information, the ST-OSCs prepared using BHJ with different weight ratios of PM6 to BTP-eC9 of 1:1.2, 0.8:1.2, 0.6:1.2, and 0.4:1.2 have the CIE (x,y) coordinates of (0.2509,0.2792), (0.2612,0.2687), (0.2733,0.2802), and (0.2832,0.2866), corresponding to different correlative color temperatures of 14 472, 13 272, 11 278, and 9729 K, respectively. It shows that the ST-OSCs with a lower PM6 content in the BHJ possess a higher AVT, having CIE (x,y) coordinates nearer to the energy white (0.325,0.3375).

To further improve the photovoltaic performance of ST-OSCs over the two competing indexes of PCE and AVT, AuNBPs-based HTL was used to enhance the NIR absorption via the near-field plasmonic enhancement and scattering effect. The transmission electron microscopy (TEM) image, taken for the AuNBPs with a length of 130 nm and a width of 35 nm, is shown in the inset in Figure 2a. The use of MNS in the active layer is not a

Table 1. Summary of photovoltaic parameters measured for the reference opaque OSCs and the control ST-OSCs, prepared using BHJ layers having different weight ratios of PM6 to BTP-eC9, with and without the AuNBPs in the HTL, and with an OCL and without OCL. The results were averaged from the measurements of ten cells.

	D:A ratio	J_{SC} [mA cm^{-2}]	Cal. J_{SC} [mA cm^{-2}]	V_{OC} [V]	FF [%]	PCE [%]	AVT [%]	LUE [%]
Opaque OSCs	1.0:1.2	26.43 ± 0.19	26.38	0.85 ± 0.01	76.60 ± 0.16	17.25 ± 0.17	–	–
	0.8:1.2	25.38 ± 0.25	24.97	0.85 ± 0.01	75.88 ± 0.23	16.37 ± 0.19	–	–
	0.6:1.2	24.55 ± 0.21	24.13	0.85 ± 0.01	72.54 ± 0.22	15.13 ± 0.23	–	–
	0.4:1.2	22.37 ± 0.34	22.02	0.84 ± 0.01	70.41 ± 0.27	13.25 ± 0.28	–	–
Control ST-OSCs	1.0:1.2	21.83 ± 0.23	21.60	0.85 ± 0.01	72.26 ± 0.23	13.36 ± 0.19	18.8	2.51
	0.8:1.2	21.17 ± 0.33	20.77	0.85 ± 0.01	70.58 ± 0.47	12.64 ± 0.28	21.4	2.70
	0.6:1.2	19.66 ± 0.27	19.33	0.84 ± 0.01	69.13 ± 0.51	11.47 ± 0.27	24.6	2.82
	0.4:1.2	18.04 ± 0.38	17.75	0.82 ± 0.01	63.30 ± 0.27	9.41 ± 0.31	26.8	2.52
AuNBPs-based ST-OSCs	1.0:1.2	22.43 ± 0.30	22.08	0.85 ± 0.01	72.97 ± 0.26	13.88 ± 0.16	18.6	2.58
	0.8:1.2	21.98 ± 0.37	21.28	0.85 ± 0.01	72.71 ± 0.33	13.52 ± 0.22	21.4	2.89
	0.6:1.2	20.87 ± 0.41	20.43	0.85 ± 0.01	71.56 ± 0.45	12.62 ± 0.36	24.5	3.09
	0.4:1.2	19.32 ± 0.44	18.77	0.83 ± 0.01	65.15 ± 0.38	10.41 ± 0.21	26.7	2.78
AuNBPs-based ST-OSCs with an OCL	0.6:1.2	21.54 ± 0.43	20.92	0.85 ± 0.01	72.16 ± 0.44	13.15 ± 0.25	25.9	3.41

perfect solution for increasing absorption in the organic photoactive layer.[55,56] In this work, we show that the use of the hybrid AuNBPs-PEDOT:PSS HTL is more favorable for achieving the NIR absorption enhancement in the ST-OSCs, optimized through a combination of theoretical simulation and experimental observations. The AuNBPs-based ST-OSCs have a layer configuration of ITO/AuNBPs-PEDOT:PSS (40 nm)/BHJ (120 nm)/BCP (8.0 nm)/Au(1.0 nm)/Ag (10 nm). The schematic structure of the AuNBPs-based ST-OSC is shown in the inset in Figure 2b. The schematic energy-level diagram of the functional materials used in this work is shown in Figure S5, Supporting Information. The work function of the hybrid AuNBPs-PEDOT:PSS HTL was analyzed using ultraviolet photoelectron spectroscopy (UPS) measurements. The work function of −5.1 eV was observed for the hybrid AuNBPs-PEDOT:PSS HTL, which is very close to that of a pristine PEDOT:PSS HTL (−5.0 eV). In this work, the concentration of the AuNBPs in the hybrid AuNBPs-PEDOT:PSS HTL was optimized experimentally for achieving the best PCE, as shown in Figure S6, Supporting Information. A volume ratio of AuNBPs solution to PEDOT:PSS solution of 1:4 optimized and adopted for making the hybrid AuNBPs-PDOT:PSS HTL. The spatial distribution of the AuNBPs in the hybrid AuNBPs-PEDOT:PSS HTL was examined using the scanning electron microscope (SEM) measurements. The SEM image measured for the hybrid AuNBPs-PEDOT:PSS HTL, prepared using an optimized volume ratio of AuNBPs to PEDOT:PSS of 1:4, is shown in Figure S7, Supporting Information. The SEM measurements reveal that the AuNBPs are randomly distributed without forming observable agglomerations in the hybrid HTL. The transmission spectra measured for a 40 nm thick pristine PEDOT:PSS layer and a 40 nm thick hybrid AuNBPs-PEDOT:PSS HTL are shown in Figure S8, Supporting Information, revealing that the hybrid AuNBPs-PEDOT:PSS HTL and the pristine PEDOT:PSS HTL have almost identical transmission behavior over the visible light range. These results suggest that the incorporation of the hybrid AuNBPs-PEDOT:PSS HTL helps the NIR absorption enhancement without changing the AVT of the ST-OSCs.

$J-V$ characteristics measured for the AuNBPs-based ST-OSCs with BHJ having different weight ratios of PM6 to BTP-eC9 are plotted in Figure S9a, Supporting Information. A summary of the performance of the ST-OSCs with a pristine PEDOT:PSS HTL and a hybrid AuNBPs-PEDOT:PSS HTL, made with the BHJ having different weight ratios of PM6 to BTP-eC9, is listed in Table 1. The use of the hybrid AuNBPs-PEDOT:PSS HTL is apparently more favorable for the efficient operation of the ST-OSCs. AuNBPs-based ST-OSTs with PCE values of 13.88%, 13.42%, 12.62%, and 10.41% were obtained for the cells with BHJ having different weight ratios of PM6 to BTP-eC9 of 1:1.2, 0.8:1.2, 0.6:1.2, and 0.4:1.2, which are evidently higher than that of the AuNBPs-free ST-OSTs with the corresponding BHJ layers. The improvement can be mainly attributed to the higher J_{SC}, due to the AuNBPs-assisted NIR absorption enhancement in the AuNBPs-based ST-OSCs. Our results reveal that AuNBPs-based ST-OSCs made, with a BHJ having a lower weight ratio of PM6 to BTP-eC9, for example, 0.6:1.2, is more preferred for improving the overall performance of the AuNBPs-based ST-OSCs over the two competing indexes of PCE and AVT. The above discussion also agrees with the examination of the LUE for different ST-OSCs, showing that AuNBPs-based ST-OSCs, made with a BHJ with a weight ratio of PM6 to BTP-eC9 of 0.6:1.2, have the highest LUE of 3.09, as shown in Figure 2a. $J-V$ characteristics measured for a control ST-OSC with a pristine PEDOT:PSS HTL and the one with an optimal hybrid AuNBPs-PEDOT:PSS HTL, prepared using the BHJ having a weight ratio of PM6 to BTP-eC9 of 0.6:1.2, are shown in Figure 2b. The corresponding EQE spectra are shown in Figure 2c, revealing clearly that the increase in EQE of the AuNBPs-based ST-OSCs over the long wavelength range from 700 to 1000 nm is mainly due to the AuNBPs-assisted NIR absorption enhancement. The EQE spectra and the transmission spectra measured for a set of the AuNBPs-based ST-OSCs prepared with the BHJ having different weight ratios of

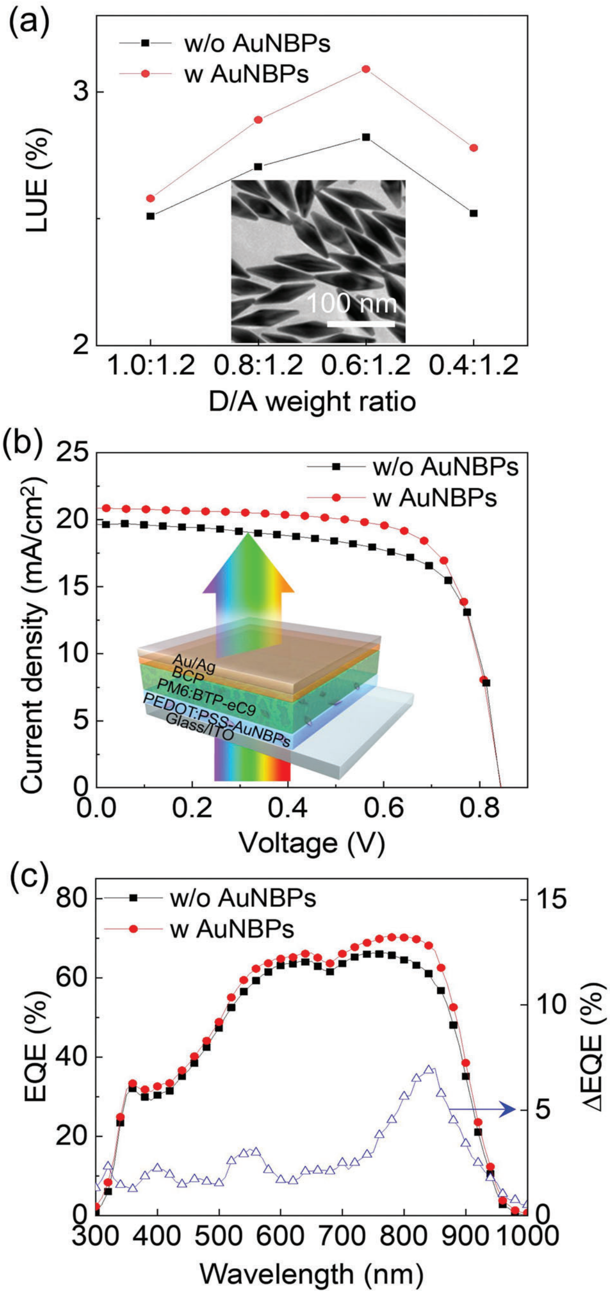

Figure 2. a) Evolution of LUE as a function of the weight ratio of PM6 to BTP-eC9 in the ST-OSC with and without AuNBPs. Inset: TEM image of AuNBPs. b) *J*–*V* characteristics of the ST-OSCs, with a BHJ having a weight ratio of PM6 to BTP-eC9 of 0.6:1.2, with and without AuNBPs. Inset: cross-sectional schematic view of the AuNBPs-based ST-OSCs. c) EQE spectra (solid symbols) measured for ST-OSCs, with a BHJ having a weight ratio of PM6 to BTP-eC9 of 0.6:1.2, with and without AuNBPs, and EQE difference (open symbols) between devices with and without AuNBPs.

PM6 to BTP-eC9 of 1:1.2, 0.8:1.2, 0.6:1.2, and 0.4:1.2 are shown in Figure S9b,c, Supporting Information.

NIR absorption enhancement in the AuNBPs-based ST-OSCs, made with a BHJ having a weight ratio of PM6 to BTP-eC9 of 0.6:1.2, has also been analyzed using the FEM simulation. The thickness values of the functional layers and upper semitransparent electrodes used in the AuNBPs-based ST-OSCs were measured using TEM. The TEM image showing the cross-section of the OSC is shown in Figure S10, Supporting Information. The measured thickness values of all layers in the OSCs were then used in the FEM simulation to obtain a better correlation between the theoretical simulation and experimental results. The wavelength-dependent refractive indexes and extinction coefficients of the functional layers used for the FEM simulation, as shown in Figure S11, Supporting Information, were measured using ellipsometer. The peak wavelength of the AuNBPs-induced LSPR is designed to matching with the absorption profile of the PM6:BTP-eC9 BHJ for achieving NIR absorption enhancement in the ST-OSCs. The distribution of the electric field intensity in the ST-OSCs with and without the presence of the AuNBPs in the HTL has been analyzed using the FEM. The simulation results, revealing the profile of the optical field at 825 nm that is close to the resonance wavelength of AuNBPs-induced LSPR, are shown in **Figure 3**. It is clear that a strong near-field enhancement around the AuNBPs penetrating inside the active layer is manifested. The AuNBPs have an antenna effect increasing the optical path of the incident light through light scattering, and thereby boosting the absorption in the active layer.[39] To gain an insight of the AuNBPs on absorption enhancement, the time averaged Poynting vector was calculated using the following equation:

$$\vec{\Pi}\ (\vec{r},\omega) = \frac{1}{2}\,\mathfrak{I}\left\{\vec{E}\,(\vec{r},\omega) \times \overrightarrow{H^{*}}\,(\vec{r},\omega)\right\} \tag{3}$$

where $\vec{H}$ is the magnetic field. The vector $\vec{\Pi}$ was calculated along the white dashed ellipsoids and the red lines, indicating the location of the extremities of the Poynting's vector starting on the ellipsoids, as shown in Figure 3b. The direction of the scattered light is perpendicular to the induced dipole and is enhanced in the forward direction of the incident light toward the active layer. The strong forward scattering is particularly large and spatially spread in the NIR, close to the longitudinal dipolar plasmon. The Poynting vector carries the effective photonic energy, revealing the significant contribution in the NIR absorption in the active layer due to the existence of the AuNBPs, which agrees with the experimental results. The simulation unveils that the optically amplified field near the vicinity of AuNBPs is mainly responsible for the NIR absorption in the active layer, realized through the excitation of LSPR, light scattering, and their mutual coupling. The AuNBPs-assisted NIR absorption enhancement contributes to the increase in the number of excitons in the active layer, leading to the improvement of the J_{SC} and the performance of the ST-OSCs.

In addition to the optical effect, the overall enhancement of photovoltaic performance can also be affected by exciton dissociation, carrier transport, and collection.[57] The photocurrent density (J_{ph})–effective voltage (V_{eff}) characteristics of the ST-OSCs with and without the AuNBPs in the HTL were measured for analyzing the effect of the AuNBPs on charge extraction properties of the ST-OSCs. The results are shown in **Figure 4**a, where $J_{\mathrm{ph}} = J_{\mathrm{l}} - J_{\mathrm{d}}$, J_{l} is the current density measured under the illumination of AM 1.5 G and J_{d} is the dark current density. The effective voltage is $V_{\mathrm{eff}} = V_0 - V_{\mathrm{a}}$, where V_0 is the built-in potential and V_{a} is the applied bias. Under a low V_{eff}, the charge recombination decreases

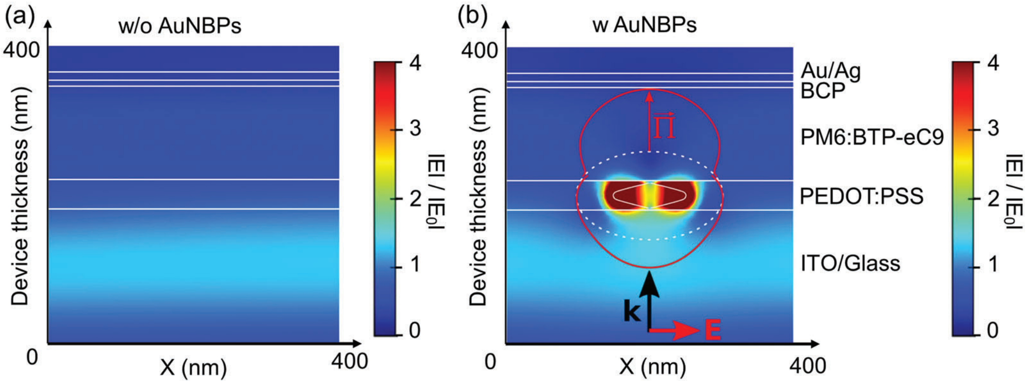

Figure 3. Distributions of the electric field intensity inside ST-OSCs with a BHJ having a weight ratio of PM6 to BTP-eC9 of 0.6:1.2, a) without AuNBPs, b) with AuNBPs at a wavelength of 825 nm. The scattering diagrams, plotted in red around AuNBPs, represent the Poynting vector $\vec{\Pi}$ along the white-dashed ellipsoids.

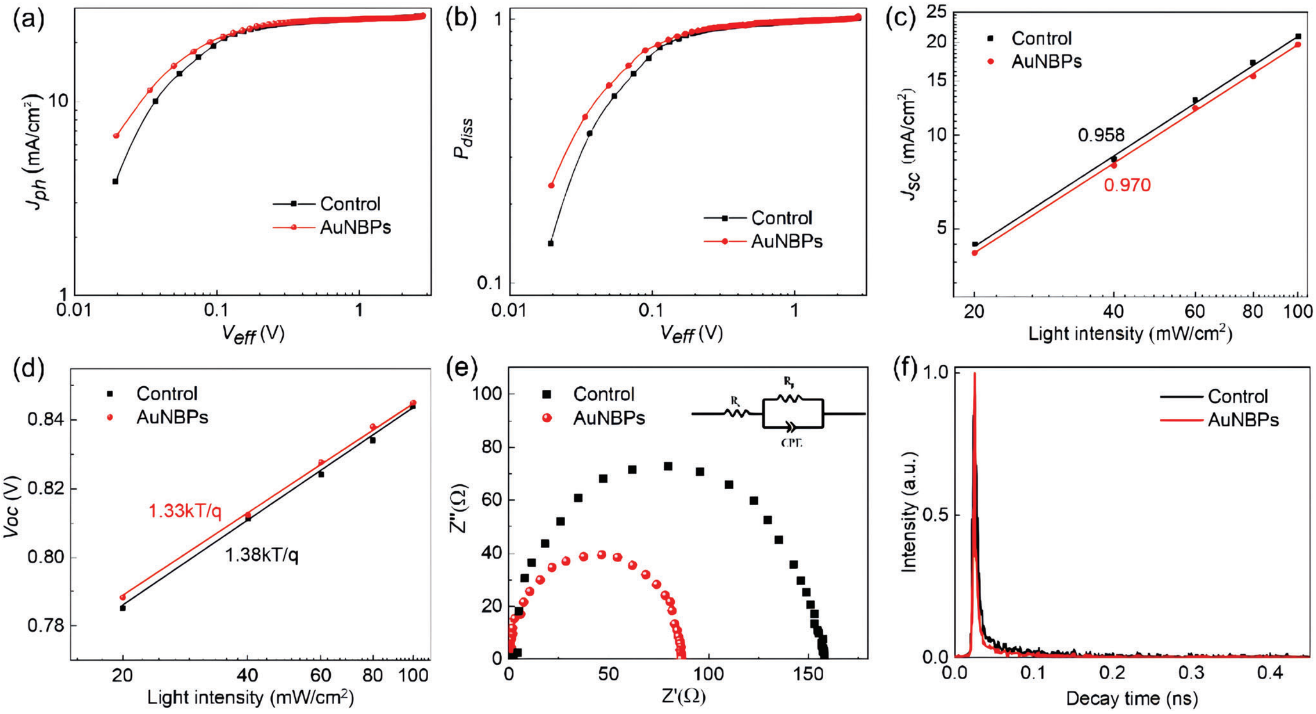

Figure 4. a) $J_{ph}-V_{eff}$, b) $P_{diss}-V_{eff}$, c) $J_{SC}-I$, d) $V_{OC}-I$ characteristics, and e) Nyquist plot under illumination at open-circuit conditions, inset: equivalent circuit model. f) TRPL spectra for control device without AuNBPs and device with AuNBPs.

with V_{eff}, therefore not all photo-generated charge carriers can be collected due to the bimolecular recombination. Under a high V_{eff} (>0.6 V), almost all the photo-generated charge carriers can be swept out and collected, generating a saturated photocurrent density (J_{sat}). In this case, the J_{ph} of a control ST-OSC with a pristine PEDOT:PSS HTL and that of the AuNBPs-based ST-OSCs saturate nearly at the same V_{eff}, but the J_{ph} of the latter is higher, indicating a more efficient exciton dissociation probability (P_{diss}) in the AuNBPs-based ST-OSCs. Under $V_{eff} < 0.3$ V, a higher P_{diss} is observed for the AuNBPs-based ST-OSCs as compared to that of a control ST-OSC with a pristine HTL, as shown in Figure 4b. The ST-OSC with a hybrid AuNBPs-PEDOT:PSS HTL has a P_{diss} of 98.5%, which is apparently higher than that of the control ST-OSC with a pristine PEDOT:PSS HTL (95.2%). We further investigated the influence of AuNBPs on the charge-carrier recombination in the devices by measuring the dependence of J_{SC} with respect to light intensity (I). J_{SC} follows a power law dependence on I, for example, $J_{SC} \propto I^{\alpha}$,[58] An exponent α of 0.97 is obtained for the AuNBPs-based ST-OSCs, which is evidently higher than that of a control ST-OSC with a pristine PEDOT:PSS HTL (0.958), as shown in Figure 4c. The higher α value of the AuNBPs-ST-OSCs reveals an improved exciton dissociation probability. $V_{OC}-I$ characteristics of the ST-OSCs were also investigated. The results are shown in Figure 4d. A slope of 1.33 kT/q is found for the AuNBPs-based ST-OSCs, which is smaller to that of a control device (1.38 kT/q), where k is the Boltzmann constant, T is the temperature

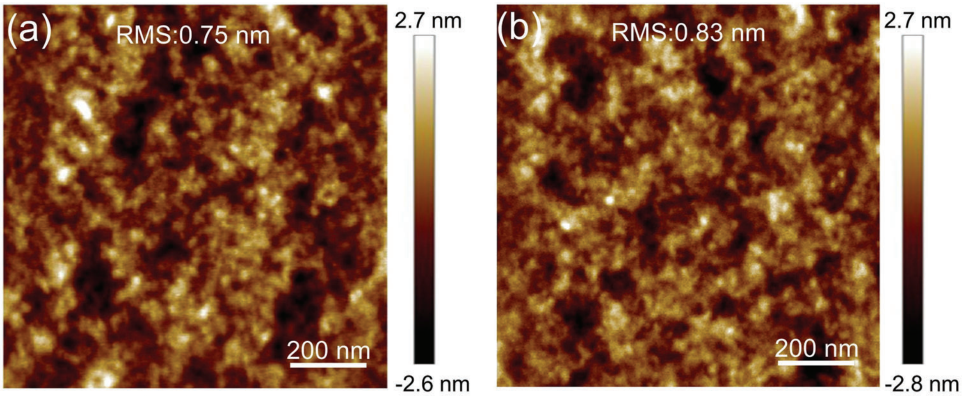

ITO/PEDOT:PSS ITO/PEDOT:PSS-AuNBPs

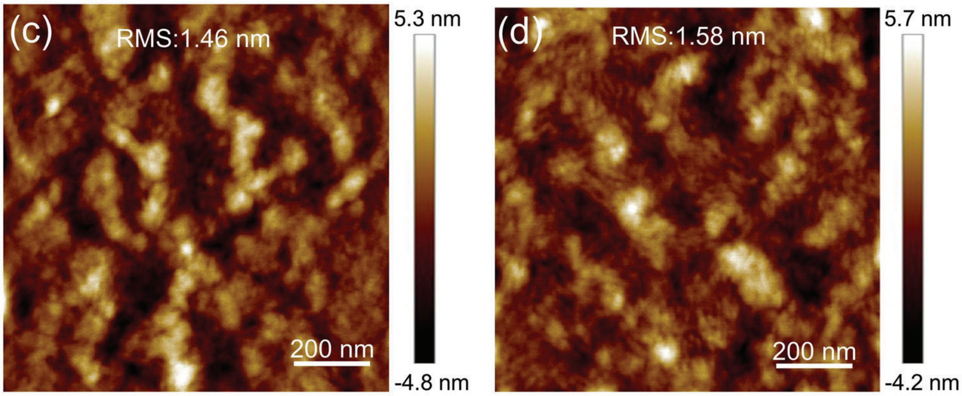

ITO/PEDOT:PSS/PM6:BTP-eC9 ITO/PEDOT:PSS-AuNBPs/PM6:BTP-eC9

Figure 5. AFM images measured for a) a pristine PEDOT:PSS HTL and b) the hybrid AuNBPs-PEDOT:PSS HTL. AFM images measured for the PM6:BTP-eC9 blend layers coated on c) a pristine PEDOT:PSS HTL, and d) the hybrid AuNBPs-PEDOT:PSS HTL.

in Kelvin, and q is the elementary charge. A reduced slope, for example, close to 1 kT/q, implies that the weaker trap-assisted recombination loss processes in the AuNBPs-ST-OSCs.[59] These results demonstrate that the incorporation of AuNBPs can help enhancing the charge extraction through mitigation of the charge recombination, and thereby yielding a higher J_{SC} and PCE.

The contact resistance and the bulk resistance of the AuNBPs-based ST-OSCs and the control ST-OSC with a pristine PEDOT:PSS HTL were analyzed using the impedance spectroscopy, measured at the open circuit condition, under the illumination. R_s, shown in the equivalent electrical circuit diagram in the inset in Figure 4e, is the contact resistance. The corresponding Nyquist plots measured for the different ST-OSCs are shown in Figure 4e, revealing the AuNBPs-based ST-OSCs having a lower bulk resistance, R_p, represented by a smaller diameter of the semicircles in the Nyquist plots. Compared to the control device, AuNBPs-based ST-OSCs have a significantly lower R_p and R_s, suggesting that the use of the hybrid AuNBPs-PEDOT:PSS HTL benefits electric properties of the cells.

The dynamics of the charge carriers in the AuNBPs-based ST-OSCs and a control ST-OSC with a pristine PEDOT:PSS HTL were analyzed using the time-resolved photoluminescence (TRPL) measurements, as shown in Figure 4f. Results show that the AuNBPs-based ST-OSCs have an exciton lifetime of 22.9 ps, which is shorter than that of a control ST-OSC with a pristine PEDOT:PSS HTL (30.4 ps). Such trend can be attributed to the strong local electric field in the vicinity of AuNBPs, enabling an efficient dissociation of the photogenerated excitons in the active layer. The TRPL results support the above discussion made with experimental results and the theoretical simulation. It shows that the use of the hybrid AuNBPs-PEDOT:PSS HTL helps mitigating the exciton quenching, which would otherwise be inevitable if the NMS were blended in the active layer. FEM simulation unveils clearly that the near-field enhancement, caused by the hybrid AuNBPs-induced LSPR in the HTL, can extend into the active layer, as shown in Figure 3b.

The surface morphological properties of the pristine PEDOT:PSS HTL, the hybrid AuNBPs-PEDOT:PSS HTL, and PM6:BTP-eC9 blend layers deposited on the pristine PEDOT:PSS HTL and the hybrid AuNBPs-PEDOT:PSS HTL were analyzed using AFM measurements. The AFM images measured for the pristine PEDOT:PSS HTL and the hybrid AuNBPs-PEDOT:PSS HTL are shown in **Figure 5**a,b. A pristine PEDOT:PSS HTL on the ITO/glass substrate has a RMS roughness of 0.75 nm, while that of the hybrid AuNBPs-PEDOT:PSS HTL on the ITO/glass has a similar RMS roughness of 0.83 nm. This suggests that the AuNBPs were well embedded in the PEDOT:PSS layer with least probability of forming a direct contact with the active layer. The large scale AFM images measured for the pristine PEDOT:PSS HTL and the hybrid AuNBPs-PEDOT:PSS HTL over an area of 10 µm by 10 µm are shown in Figure S12, Supporting Information. The AFM measurements show that the pristine PEDOT:PSS

HTL and the hybrid AuNBPs-PEDOT:PSS HTL have comparable RMS roughness, agreeing with the SEM measurements (Figure S7, Supporting Information) in showing that the AuNBPs are well embedded in the hybrid HTL. The AFM images measured for the PM6:BTP-eC9 blend layers coated on the pristine PEDOT:PSS HTL and the hybrid AuNBPs-PEDOT:PSS HTL are shown in Figure 5c,d, revealing that the formation of the domain feature of the PM6:BTP-eC9 blend layers. The PM6:BTP-eC9 blend layer formed on the surface of the hybrid AuNBPs-PEDOT:PSS HTL has a RMS roughness of 1.58 nm, which is comparable to that of the blend layer formed on the pristine PEDOT:PSS HTL (1.46 nm). The stability of the ST-OSCs made with different HTLs was examined using the aging test over a period of 14 days, as shown in Figure S13, Supporting Information. The results show that the AuNBPs-based ST-OSCs and a control ST-OSC with a pristine PEDOT:PSS HTL have comparable cell stability, demonstrating the suitability and advantage of the solution-processable AuNBPs-PEDOT:PSS HTL for use in high-performance ST-OSCs.

In addition to the NIR absorption enhancement in BHJ using AuNBPs-induced LSPR, a low/high dielectric constant LiF (150 nm)/MoO_3 (100 nm) double layer OCL was used to further improve the performance of the ST-OSCs over the two competing indexes of PCE and AVT. A 150 nm thick LiF has a low refractive index of 1.39, and a 100 nm thick MoO_3 layer has a high refractive index of 2.1, as shown in Figure S11, Supporting Information. The thickness combination of the low/high dielectric constant double layer LiF (150 nm)/MoO_3 (100 nm) OCL was optimized for the AuNBPs-based ST-OSCs. Contour maps of the integrated transmittance calculated for the ST-OSCs as functions of the LiF layer thickness and the MoO_3 layer thickness in the double dielectric OCL over the wavelength ranges from 370 to 740 nm and from 740 to 1000 nm are shown in **Figure 6**a,b. Contour map of the absorption calculated for the PM6:BTP-eC9 (0.6:1.2) BHJ in the ST-OSCs as functions of the LiF layer thickness and the MoO_3 layer thickness in the double dielectric OCL over the wavelength range from 370 to 1000 nm is shown in Figure 6c. The simulation reveals clearly that a combination of LiF (150 nm)/MoO_3 (100 nm) low/high dielectric constant double layer OCL arouses evident optical phenomena, allowing visible light to pass through, and long wavelength light, for example, NIR light, to absorb to the BHJ. The distributions of the electric field intensity calculated for a control ST-OSC with an OCL and without the OCL are shown in Figure S14, Supporting Information. The results reveal that the use of a low/high dielectric constant LiF (150 nm)/MoO_3 (100 nm) double layer OCL assists in simultaneous improved visible light transparency and enhanced NIR absorption.

J–V characteristics measured for the optimized AgNBPs-based ST-OSCs with an OCL and without OCL are shown in **Figure 7**a. The cross-sectional schematic diagram illustrating the cross-sectional view of an AuNBPs-based ST-OSC with a LiF/MoO_3 double layer OCL is shown in the inset in Figure 7a. Transmission spectra measured for the AgNBPs-based ST-OSCs with an OCL and without OCL are shown in Figure 7b. The EQE spectra of ST-OSCs with an OCL and without OCL are shown in Figure S15a, Supporting Information. The quantum utilization ef-

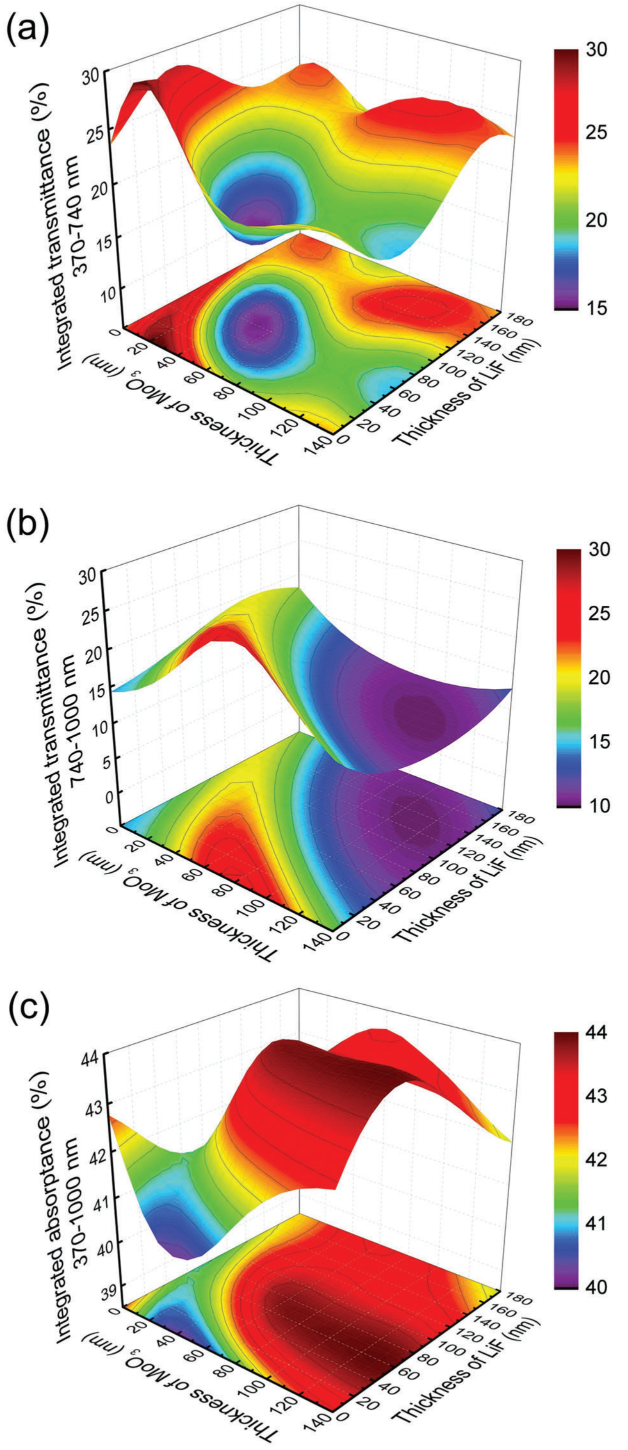

Figure 6. Contour maps of the integrated transmittance calculated for the ST-OSCs as functions of the LiF layer thickness and the MoO_3 layer thickness in the double dielectric OCL over the wavelength ranges from a) 370 to 740 nm, and b) 740 to 1000 nm. c) Contour map of the absorption calculated for the PM6:BTP-eC9 (0.6:1.2) BHJ in the ST-OSCs as functions of the LiF layer thickness and the MoO_3 layer thickness in the double dielectric OCL over the wavelength range from 370 to 1000 nm.

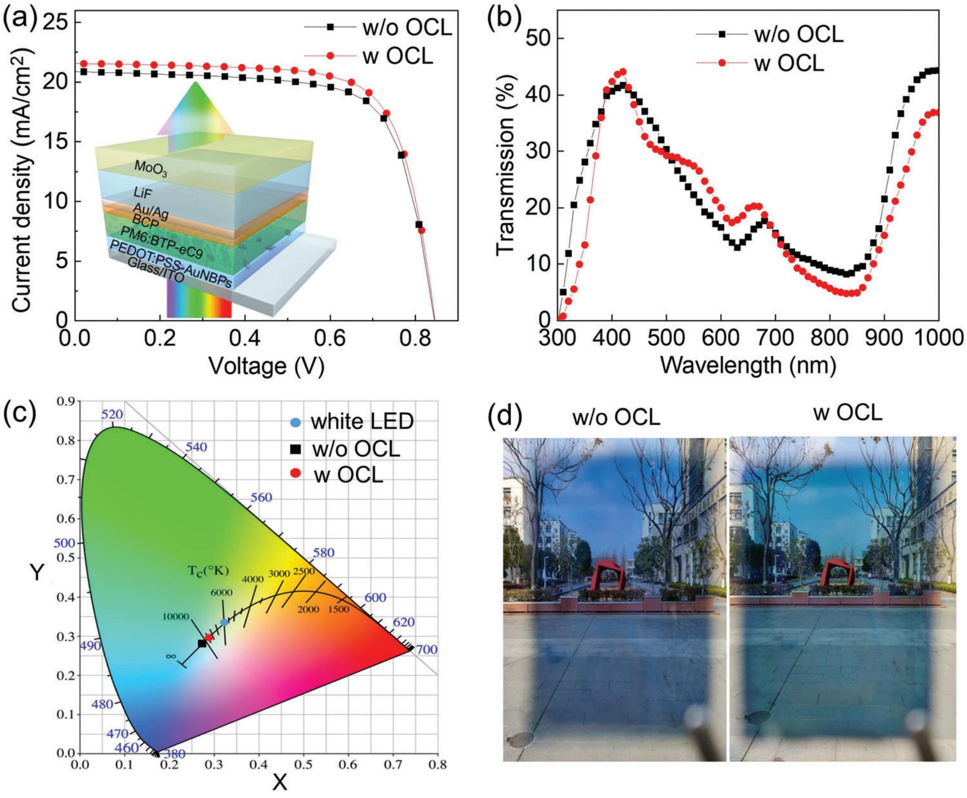

Figure 7. a) *J*–*V* characteristics, b) transmission spectra, and c) CIE (*x*,*y*) coordinates of the optimized AgNBPs-based ST-OSCs with an OCL and without OCL. Inset in (a): schematic diagram illustrating the cross-sectional view of an AuNBPs-based ST-OSC with a LiF/MoO_3 double layer OCL. d) Photo pictures taken for the AgNBPs-based ST-OSCs with an OCL and without OCL.

ficiency (QUE), a figure of merit of ST-OSCs, was calculated to evaluate the light utilization of the ST-OSCs. QUE is defined by:

$$\mathrm{QUE}(\lambda) = \mathrm{EQE}(\lambda) + T(\lambda) \tag{4}$$

The QUE spectra of the AuNBPs-based ST-OSCs with an OCL and without OCL are shown in Figure S15b, Supporting Information, revealing that the ST-OSCs developed in this work possess an average QUE of 80% over the wavelength range from visible to NIR light. The transmission spectrum measured for the ITO/glass substrate is shown in Figure S15b, Supporting Information for comparison. CIE (*x*,*y*) coordinates of the optimized AgNBPs-based ST-OSCs with an OCL and without OCL are shown in Figure 7c. The CIE (*x*,*y*) coordinates of the ST-OSCs with an OCL shift toward the equal energy white in the CIE chromaticity diagram. Photo pictures taken for the AgNBPs-based ST-OSCs with an OCL and without OCL are shown in Figure 7d. The experimental results reveal clearly that the use of an optimized LiF (150 nm)/MoO_3 (100 nm) double layer OCL enables a simultaneous improvement in PCE and AVT of the ST-OSCs, leading to a PCE of 13.15%, which is evidently higher than that of a control ST-OSC without the OCL (12.62%). An impressive high AVT of 25.9% was obtained for the AgNBPs-based ST-OSCs with a low/high dielectric constant double layer OCL, which is clearly higher than that of a control ST-OSC without the OCL (24.5%). The effect of a bilayer dielectric LiF/MoO_3 OCL on the stability of the ST-OSCs was also examined using the same aging test, the results are shown in Figure S16, Supporting Information. An obvious improvement in the stability of the ST-OSCs with a bilayer dielectric LiF/MoO_3 OCL is observed as compared to that of the ST-OSCs without OCL. In addition to the desired optical effect, a bilayer dielectric LiF/MoO_3 OCL also acts an upper barrier layer for retarding the permeation of the moisture and oxygen to the active layer, favoring the efficient and stable operation of the ST-OSCs. In this work, an impressive record LUE of 3.41% is obtained for the ST-OSCs, demonstrating the unique advantage of incorporating the hybrid AgNBPs-PEDOT:PSS HTL and the low/high dielectric constant double OCL for application in high-performance ST-OSCs. The corresponding photovoltaic parameters measured for the reference opaque PM6:BTP-eC9-based OSCs, the control ST-OSCs and the AuNBPs-based ST-OSCs with an OCL and without the OCL, prepared using the BHJ layers having different weight ratios of PM6 to BTP-eC9, are listed in Table 1. A summary of the PCE and LUE results of the ST-OSCs reported by different groups is shown in Figure S17, Supporting Information.

The performance of the ST-OSCs has been optimized over the two competing index of PCE and AVT, through incorporating a hybrid AuNBPs-PEDOT:PSS HTL and a low/high dielectric constant double layer OCL. ST-OSC technology can be advanced through continuous development of novel organic photoactive materials with extended absorption in long wavelengths. The results and the design approach of the ST-OSCs presented in this work provide new ideas and process know-how to the fast-growing field of OSCs. The high-performance ST-OSCs would offer potentially more opportunities for applications in new markets such as mobile electronics, smart sensors, automotive, power generating windowpanes, greenhouses, and outdoor lifestyle.

3. Conclusions

In summary, theoretical simulation, experimental optimization, and process integration were used to maximize the LUE of the ST-OSCs. We have applied a new hybrid AuNBPs-PEDOT:PSS-based HTL together with a low/high dielectric constant double layer OCL to improve the performance of the ST-OSCs over the two competing indexes of PCE and AVT. A PCE of 13.15% and an AVT of 25.9% were obtained for the AuNBPs-based ST-OSCs, realized through combined effect of AuNBPs-induced LSPR, light scattering and the optical coupling of a bilayer LiF/MoO_3 OCL. The results of this work are very encouraging, providing a practical approach for development of high-performance ST-OSCs.

4. Experimental Section

Materials: The AuNBPs solution (from NanoSeedz) was used as received. The AuNBPs have a length of 135 nm and a width of 35 nm. The PEDOT:PSS solution (Clevios PVP 4083) was purchased from Heraeus. PM6 and BTP-eC9 (from Solarmer) were used as received. Chloroform and 1-chloronaphthalene were obtained from Sigma Aldrich. All chemicals and regents used in this work were used as received without purification.

Device Fabrication: The ITO/glass substrates with a sheet resistance of 15 Ω sq^{-1} were cleaned by ultrasonication sequentially with detergent, acetone, isopropyl alcohol, and deionized water each for 30 min. After the wet cleaning, the ITO/glass substrates were exposed to ozone treatment for 15 min. The volume ratio of the AuNBPs solution to the PEDOT:PSS solution in the AuNBPs-PEDOT:PSS mixture solution was optimized and prepared by stirring for improving the miscibility between AuNBPs and PEDOT:PSS. A 40 nm thick hybrid AuNBPs-PEDOT:PSS HTL was formed on the ITO/glass substrates by spin-coating at a rotation speed of 3000 rpm for 60 s, followed by annealing at 130 °C for 20 min in air. The PM6:BTP-eC9 solutions with different weight ratios of PM6 to BTP-eC9 were dissolved in chloroform, with a 0.5% of 1-chloronaphthalene solvent additive, forming different precursor solutions with a concentration of 16 mg mL^{-1}. A 120 nm thick active layer was deposited on the HTL by spin-coating at a rotation speed of 2500 rpm for 30 s, following by an annealing at 110 °C for 10 min in a glove box with O_2 and H_2O levels < 0.1 ppm. An 8.0 nm thick BCP ETL was deposited on the BHJ by thermal evaporation in a vacuum system, with a base pressure of $<10^{-6}$ Pa. The upper metal contacts, for example, a 100 nm thick Al for opaque OSCs and a bilayer Au (1.0 nm)/Ag (10 nm) semitransparent cathode for ST-OSCs, were deposited by thermal evaporation. The bilayer LiF (150 nm)/MoO_3 (100 nm) dielectric OCL was deposited on the top of the upper semitransparent electrode using thermal evaporation. The OSCs have an active area of 4.0 mm^2, defined by the overlapped area between the ITO contact and the upper metal contact.

Characterization: *J–V* characteristics of the OSCs were measured using a calibrated AM 1.5 G solar simulator (ABET Sun2000) (100 mW cm^{-2}). EQE spectra of the OSCs were measured using a 7-SCSpec solar cell measurement system (7-STAR Co.). The ST-OSCs were stored in N_2-purged glove box with moisture and oxygen levels below 0.1 ppm. The stability of the ST-OSCs was measured by monitoring the performance of the cells in air in the lab, with a typical relative humidity of ≈40 RH% at room temperature. The CIE 1931 color coordinate of ST-OSCs were obtained using a PR-655 spectroradiometer (Photo Research). The transmission and absorption spectra of the functional layers and the ST-OSCs were measured using a UV–vis spectrophotometer (HITACHI Ue3900H). Time-resolved PL spectra were measured using an FLSP 920 fluorescence spectrometer. The work function of the PEDOT:PSS and the hybrid AuNBPs-PEDOT:PSS layers were measured using the ESCA microprobe (PHI5000 VersaProbe III). Impedance spectroscopy was measured using an impedance analyzer (Corrtest CS2350H) with a bias of 0.8 V over the frequency range from 0.1 Hz to 1 MHz. The surface morphological properties of different films were analyzed using SEM (HITACHI S-4800) and AFM (Nanonavi SPA-400SPM). The TEM samples were prepared by a focused ion beam setup (Dualbeam FEI Helios Nanolab 660). TEM images of the samples were analyzed using a double corrected (probe and imaging) JEOL ARM200F microscope equipped with a cold FEG (Field Emission Gun) source operated at 200 kV.

Theoretical Simulation: The optical profiles in different OSCs, comprising the layer configuration of glass (semi-infinite)/ITO (150 nm)/HTL (40 nm, AuNBPs-PEDOT:PSS or PEDOT:PSS)/PM6:BTP-eC9 (120 nm)/BCP (8 nm)/Au (1.0 nm)/Ag (10 nm), were calculated using the Comsol Multiphysics. Refractive indexes of the ITO, LiF, MoO_3, Au, and Ag layers were taken from refractiveindex.info database. The optical constants of the PM6:BTP-eC9 blend layer with a weight ratio of PM6 to BTP-eC9 of 0.6:1.2, PEDOT:PSS and AuNBPs-PEDOT:PSS layers were obtained using ellipsometer (J.A. Woollam RC2-XI) measurements. In the simulation, AuNBPs were considered locating in the middle of the PEDOT:PSS layer, with the geometrical parameters observed experimentally. The system was illuminated in normal incidence from the glass semi-infinite space and polarized either along *X*-axis. The distributions of the electric field and light scattering diagram in the active layer over the NIR wavelength range were calculated.

Supporting Information

Supporting Information is available from the Wiley Online Library or from the author.

Acknowledgements

This work was supported by National Natural Science Foundation of China (12174244) and Natural Scientific Foundation of Shanghai (19ZR1419500). S.W. acknowledges the funding support from the Program for Professor of Special Appointment (Eastern Scholar) at the Shanghai Institutions of Higher Learning and the Shanghai Rising-Star Program (19QA1403800). R.B. thanks the French Ambassy in China for financial support through the program "Soutien aux structures conjointes de recherche franco-chinoises Thématiques prioritaires COMIX." F.Z. thanks the support by the Research Grants Council, Hong Kong Special Administrative Region, China (12302419, C5037-18GF, and N_HKBU201/19).

Conflict of Interest

The authors declare no conflict of interest.

Data Availability Statement

The data that support the findings of this study are available in the supplementary material of this article.

Keywords

bilayer dielectric optical coupling layer, gold nanobipyramids, near-infrared, plasmonic effect, semitransparent organic solar cells

Received: April 13, 2022
Revised: June 11, 2022
Published online: July 17, 2022

[1] Z. He, B. Xiao, F. Liu, H. Wu, Y. Yang, S. Xiao, C. Wang, T. P. Russell, Y. Cao, *Nat. Photonics* **2015**, *9*, 174.
[2] S. Wang, Y. Zhao, H. Lian, C. Peng, X. Yang, Y. Gao, Y. Peng, W. Lan, O. I. Elmi, D. Stiévenard, B. Wei, F. R. Zhu, T. Xu, *Nanophotonics* **2019**, *8*, 297.
[3] T. Xu, C. Gong, S. Wang, H. Lian, W. Lan, G. Lévêque, B. Grandidier, J. Plain, R. Bachelot, B. Wei, F. R. Zhu, *Sol. RRL* **2020**, *4*, 1900522.
[4] W. Lan, J. Gu, S. Wu, Y. Peng, M. Zhao, Y. Liao, T. Xu, B. Wei, L. M. Ding, F. R. Zhu, *EcoMat* **2021**, *3*, e12314.
[5] X. Gu, Y. Wei, X. Liu, N. Yu, L. Li, Z. Han, J. Gao, C. Li, Z. Wei, Z. Tang, X. Zhang, H. Huang, *Sci. China: Chem.* **2022**, *65*, 926.
[6] Y. Liu, B. Liu, C. Ma, F. Huang, G. Feng, H. Chen, J. Hou, L. Yan, Q. Wei, Q. Luo, Q. Bao, W. Ma, W. Liu, W. Li, X. Wan, X. Hu, Y. Han, Y. Li, Y. Zhou, Y. Zou, Y. Chen, Y. Li, Y. Chen, Z. Tang, Z. Hu, Z. Zhang, Z. Bo, *Sci. China: Chem.* **2022**, *65*, 2248.
[7] Y. W. Wang, W. X. Lan, N. Li, Z. J. Lan, Z. Li, J. N. Jia, F. R. Zhu, *Adv. Energy Mater.* **2019**, *9*, 1900157.
[8] C. Li, J. Zhou, J. Song, J. Xu, H. Zhang, X. Zhang, J. Guo, L. Zhu, D. Wei, G. Han, J. Min, Y. Zhang, Z. Xie, Y. Yi, H. Yan, F. Gao, F. Liu, Y. Sun, *Nat. Energy* **2021**, *6*, 605.
[9] P. Bi, S. Zhang, Z. Chen, Y. Xu, Y. Cui, T. Zhang, J. Ren, J. Qin, L. Hong, X. Hao, J. Hou, *Joule* **2021**, *5*, 2408.
[10] L. Hong, H. Yao, Y. Cui, P. Bi, Y. Cui, T. Zhang, Y. Cheng, Y. Zu, J. Qin, R. Yu, Z. Ge, J. Hou, *Adv. Mater.* **2021**, *33*, 2103091.
[11] M. Zhang, L. Zhu, G. Zhou, T. Hao, C. Qiu, Z. Zhao, Q. Hu, B. Larson, H. Zhu, Z. Ma, Z. Tang, W. Feng, Y. Zhang, T. Russell, F. Liu, *Nat. Commun.* **2021**, *12*, 309.
[12] J. Huang, D. Zhao, Z. Dou, Q. Fan, N. Li, S. Peng, H. Liu, Y. Jiang, J. Yu, C.-Z. Li, *Energy Environ. Sci.* **2021**, *14*, 3010.
[13] J. Qin, L. Zhang, C. Zuo, Z. Xiao, Y. Yuan, S. Yang, F. Hao, M. Cheng, K. Sun, Q. Bao, Z. Bin, Z. Jin, L. Ding, *J. Semicond.* **2021**, *41*, 010501.
[14] C. Duan, L. Ding, *Sci. Bull.* **2020**, *65*, 1231.
[15] Y. P. Xie, Y. Cai, L. Zhu, R. X. Xia, L. L. Ye, X. Feng, H. L. Yip, F. Liu, G. H. Lu, S. T. Tan, Y. M. Sun, *Adv. Funct. Mater.* **2020**, *30*, 2002181.
[16] Y. G. Liu, P. Cheng, T. F. Li, R. Wang, Y. W. Li, S. Y. Chang, Y. Zhu, H. W. Chen, K. H. Wei, X. W. Zhan, B. Q. Sun, Y. Yang, *ACS Nano* **2019**, *13*, 1071.
[17] Z. H. Hu, J. Wang, X. L. Ma, J. H. Gao, C. Y. Xu, K. X. Yang, Z. Wang, J. Zhang, F. J. Zhang, *Nano Energy* **2020**, *78*, 105376.
[18] W. Song, B. Fanady, R. X. Peng, L. Hong, L. R. Wu, W. X. Zhang, T. T. Yan, T. Wu, S. H. Chen, Z. Y. Ge, *Adv. Energy Mater.* **2020**, *10*, 2000136.
[19] X. Huang, J. Oh, Y. J. Cheng, B. Huang, S. Ding, Q. He, F. Wu, C. Yang, L. Chen, Y. Cheng, *J. Mater. Chem. A* **2021**, *9*, 5711.
[20] Z. H. Hu, J. Wang, Z. Wang, W. Gao, Q. S. An, M. Zhang, X. L. Ma, J. X. Wang, J. L. Miao, C. L. Yang, F. J. Zhang, *Nano Energy* **2019**, *55*, 424.
[21] C. Xu, K. Jin, Z. Xiao, Z. Zhao, X. Ma, X. Wang, J. Li, W. Xu, S. Zhang, L. Ding, F. Zhang, *Adv. Funct. Mater.* **2021**, *31*, 2107934.
[22] C. Zhu, H. Huang, Z. R. Jia, F. F. Cai, J. Li, J. Yuan, L. Meng, H. J. Peng, Z. J. Zhang, Y. P. Zou, Y. F. Li, *Sol. Energy* **2020**, *204*, 660.
[23] W. Song, Y. X. Liu, B. Fanady, Y. F. Han, L. Xie, Z. Y. Chen, K. B. Yu, X. Peng, X. L. Zhang, Z. Y. Ge, *Nano Energy* **2021**, *86*, 106044.
[24] X. Ma, Z. Xiao, Q. An, M. Zhang, Z. Hu, J. Wang, L. Ding, F. Zhang, *J. Mater. Chem. A* **2018**, *6*, 21485.
[25] Y. W. Wang, J. Y. Han, L. F. Cai, N. Li, Z. Li, F. R. Zhu, *J. Mater. Chem. A* **2020**, *8*, 21255.
[26] H. Hu, Z. Wang, S. An, F. J. Zhang, *Sci. Bull.* **2020**, *65*, 131.
[27] C. Chueh, S. Chien, H. Yip, J. Salinas, C. Li, K. Chen, F. Chen, W. Chen, A. K. Y. Jen, *Adv. Energy Mater.* **2013**, *3*, 417.
[28] J. Min, C. Bronnbauer, Z. Zhang, C. Cui, Y. Luponosov, I. Ata, P. Schweizer, T. Przybilla, F. Guo, T. Ameri, K. Forberich, E. Spiecker, P. Bauerle, S. A. Ponomarenko, Y. Li, C. J. Brabec, *Adv. Funct. Mater.* **2016**, *26*, 4543.
[29] Y. Song, S. Chang, S. Gradecak, J. Kong, *Adv. Energy Mater.* **2016**, *6*, 1600847.
[30] J. Czolk, A. Puetz, D. Kutsarov, M. Reinhard, U. Lemmer, A. Colsmann, *Adv. Energy Mater.* **2013**, *3*, 386.
[31] Y. M. Bai, C. Y. Zhao, X. H. Chen, S. Zhang, S. Q. Zhang, T. Hayat, A. Alsaedi, Z. A. Tan, J. H. Hou, Y. F. Li, *J. Mater. Chem. A* **2019**, *7*, 15887.
[32] D. Wang, R. Qin, G. Q. Zhou, X. Li, R. X. Xia, Y. H. Li, L. L. Zhang, H. M. Zhu, X. H. Lu, L. Yip, H. Z. Chen, C. Z. Li, *Adv. Mater.* **2020**, *32*, 2001621.
[33] P. Yin, Z. Yin, Y. L. Ma, Q. Zheng, *Energy Environ. Sci.* **2020**, *13*, 5177.
[34] Z. Hu, J. Wang, X. Ma, J. Gao, C. Xu, X. Wang, X. Zhang, Z. Wang, F. Zhang, *J. Mater. Chem. A* **2021**, *9*, 6797.
[35] Y. Chang, X. Zhu, L. Zhu, Y. Wang, C. Yang, X. Gu, Y. Zhang, J. Zhang, K. Lu, X. Sun, Z. Wei, *Nano Energy* **2021**, *86*, 106098.
[36] K. Ueno, T. Oshikiri, Q. Sun, X. Shi, H. Misawa, *Chem. Rev.* **2018**, *118*, 2955.
[37] K. Chan, M. Wright, N. Elumalai, A. Uddin, S. Pillai, *Adv. Opt. Mater.* **2017**, *5*, 1600698.
[38] Y. H. Jang, Y. J. Jang, S. Kim, L. N. Quan, K. Chung, D. H. Kim, *Chem. Rev.* **2016**, *116*, 14982.
[39] Y. Oh, J. W. Lim, J. G. Kim, H. Wang, B. H. Kang, Y. W. Park, H. Kim, Y. J. Jang, J. Kim, D. H. Kim, B. K. Ju, *ACS Nano* **2016**, *10*, 10143.
[40] C. Ma, C. Liu, J. Huang, Y. Ma, Z. Liu, L.-J. Li, T. D. Anthopoulos, Y. Han, A. Fratalocchi, T. Wu, *Sol. RRL* **2019**, *3*, 1900138.
[41] S. Wu, Y. Li, H. Lian, G. Leveque, B. Grandidier, P. M. Adam, D. Gerard, R. Bachelot, T. Xu, B. Wei, *Nanotechnology* **2020**, *31*, 375203.
[42] A. Ng, W. K. Yiu, Y. Foo, Q. Shen, A. Bejaoui, Y. Zhao, H. C. Gokkaya, A. B. Djurisic, J. A. Zapien, W. K. Chan, C. Surya, *ACS Appl. Mater. Interfaces* **2014**, *6*, 20676.
[43] X. Li, W. C. H. Choy, H. Lu, W. E. I. Sha, A. H. P. Ho, *Adv. Funct. Mater.* **2013**, *23*, 2728.
[44] S. Chen, Y. j. Wang, Q. Liu, G. Shi, Z. Liu, K. Lu, L. Han, X. Ling, H. Zhang, S. Cheng, W. Ma, *Adv. Energy Mater.* **2018**, *8*, 1701194.
[45] J. Li, Y. Bai, B. Yang, J. Zhang, X. Chen, T. Hayat, A. Alsaedi, Y. Yang, J. Hou, Z. A. Tan, *J. Mater. Chem. A* **2019**, *7*, 2667.
[46] W. X. Lan, Y. W. Wang, J. Singh, F. R. Zhu, *ACS Photonics* **2018**, *5*, 1144.
[47] D. Wang, R. Qin, G. Zhou, X. Li, R. Xia, Y. Li, L. Zhan, H. Zhu, X. Lu, H. Yip, H. Chen, C. Z. Li, *Adv. Mater.* **2020**, *32*, 2001621.
[48] Y. Li, C. Ji, X. Huang, S. Hou, C. Z. Li, L. S. Liao, L. J. Guo, S. Forrest, *Adv. Mater.* **2019**, *31*, 1903173.
[49] R. Xia, C. J. Brabec, H. Yip, Y. Cao, *Joule* **2019**, *3*, 2241.
[50] C. Sun, R. Xia, H. Shi, H. Yao, X. Liu, J. Hou, F. Huang, H. Yip, Y. Cao, *Joule* **2018**, *2*, 1816.
[51] G. Ng, E. L. Kietzke, T. Kietzke, L. W. Tan, P. K. Liew, F. R. Zhu, *Appl. Phys. Lett.* **2007**, *90*, 103505.
[52] Y. Huo, X. T. Gong, T. -K. Lau, T. Xiao, C. Yan, X. G. LuLu, X. Zhan, H. L. Zhang, *Chem. Mater.* **2018**, *30*, 8661.
[53] Y. Cai, Y. Li, R. Wang, H. Wu, Z. Chen, J. Zhang, Z. Ma, X. Hao, Y. Zhao, C. Zhang, F. Huang, Y. M. Sun, *Adv. Mater.* **2021**, *33*, 2101733.
[54] Z. Yin, J. Wei, C. Chen, D. Cai, Y. Ma, M. Wang, Q. Zheng, *J. Mater. Chem. A* **2017**, *5*, 3888.
[55] H. Choi, J. P. Lee, S. J. Ko, J. W. Jung, H. Park, S. Yoo, O. Park, J. R. Jeong, S. Park, J. Y. Kim, *Nano Lett.* **2013**, *13*, 2204.
[56] A. T. Nair, S. P. Palappra, V. S. Reddy, *ACS Appl. Mater. Interfaces* **2018**, *10*, 32483.
[57] S. W. Baek, J. Hun Kim, J. Kang, H. Lee, J. Young Park, J. Y. Lee, *Adv. Energy Mater.* **2015**, *5*, 1501393.
[58] Y. W. Wang, B. Wu, Z. H. Wu, Z. J. Lan, Y. F. Li, M. J. Zhang, F. R. Zhu, *J. Phys. Chem. Lett.* **2017**, *8*, 5264.
[59] H. Cho, S. H. Jeong, M. H. Park, Y.-H. Kim, C. Wolf, C. L. Lee, J. H. Heo, A. Sadhanala, N. Myoung, S. Yoo, S. H. Im, R. H. Friend, T. W. Lee, *Science* **2015**, *350*, 1222.